IEEE Access
Multidisciplinary | Rapid Review | Open Access Journal

Received 31 October 2023, accepted 4 December 2023, date of publication 7 December 2023,
date of current version 14 December 2023.

Digital Object Identifier 10.1109/ACCESS.2023.3340861

RESEARCH ARTICLE

Multivariate Cooperative Internal Mode Control of RBF Neural Network for Power System Chaos Suppression

ZHIPENG LIU[1], YUCHEN ZHANG[2], SHIJIE YANG[3], AND YANLING LYU[2]
[1]State Grid Heilongjiang Electric Power Company Ltd., Electric Power Research Institute, Harbin 150000, China
[2]School of Electrical and Electronic Engineering, Harbin University of Science and Technology, Harbin 150080, China
[3]State Grid Ezhou Echeng District Power Supply Company Ltd., Ezhou 436000, China

Corresponding author: Yuchen Zhang (xiaobai1994@gmail.com)

This work was supported in part by State Grid Heilongjiang Electric Power Company Ltd., Electric Power Research Institute, under Grant 52243723000B.

ABSTRACT In this paper, a multivariate cooperative internal mode control method based on RBF neural network (RBF-NN) inverse system is proposed to suppress the chaotic behavior in the power system. Firstly, a seven-dimensional model of the controlled power system including energy storage (ES) and static var compensator (SVC) is constructed, and the chaotic dynamics of the system is analyzed by local bifurcation diagram, attractor phase diagram and timing diagram, and the merging crisis and coexistence of chaotic attractors are found in the power system under the action of the low-frequency power disturbance. Secondly, considering the parameter uncertainties of the power system, an RBF-NN inverse system model of the controlled power system is established based on inverse system theory and neural network theory to realize its pseudo-linearization, and a multivariable cooperative internal mode controller is designed to suppress the chaotic behavior in the power system by combining the ES and the SVC. Finally, the effectiveness and robustness of the proposed chaos suppression control strategy are verified by simulation.

INDEX TERMS Chaos, chaos suppression, internal mode control, power system, RBF neural network.

I. INTRODUCTION

CHAOTIC behavior is a complex dynamical phenomenon unique to nonlinear systems, manifested as broadband pseudo-random oscillations, which is widespread in nature and human society [1], [2]. As a typical complex system with multivariable and multiparameter characteristics, the high degree of nonlinearity and uncertainty brings a rich dynamic behavior to the power system, which is highly susceptible to chaotic oscillations when the unit or load changes its parameters or is subjected to external disturbances, leading to voltage instability or even collapse, and therefore, chaotic oscillations potentially threaten the safe and stable operation of the power system [3], [4], [5], [6], [7].

In recent years, with the increasing complexity of power system structure and electrical equipment application, the analysis and suppression of chaos oscillation in the power system has gradually become a research hotspot in the power industry. Zhou et al. [8] established a second-order power system model with Lewschitz dynamic damping model, and pointed out that the chaos band of the system is affected by the varying damping parameters. Reference [9] investigated the chaos behavior in the three-dimensional model of the power system, and found that the system with reduced damping coefficient experienced a variety of chaos oscillation modes. Reference [10] found that the amplitude and frequency of the electromagnetic power disturbance or load disturbance can affect the sudden chaos oscillation in the fourth-order power system model considering the excitation limiting links. In addition, Li et al. [11] conducted a chaos analysis on the six-dimensional model of the three-bus power system, which showed that due to the increase of load, the critical chaos oscillation tends to occur when the system is closer to the stable operation limit. Meanwhile, Ai et al. [12] generated chaotic oscillations in a six-dimensional model of the power system by mechanical input power and model order, and proposed a state transition algorithm based on

The associate editor coordinating the review of this manuscript and approving it for publication was Nagesh Prabhu.

the lens imaging learning strategy to estimate the parameters of the chaotic model of the power system and reproduce its chaotic behaviour. Reference [13] analyzed the chaos of the seven-dimensional power system model by the input mechanical power, and showed that there is a strong correlation between the power parameters and the chaos behavior. In addition, Ni et al. [14] proposed a fast fixed-time non-singular terminal sliding mode control method to achieve the chaos control goal in a fixed time. Then, Cao et al. [15] proposed a method of dynamic surface sliding mode control, which reduces the design steps of dynamic surface controllers and the complexity of stability analysis, and effectively suppress the chaotic oscillations in power system. Reference [16] optimized the sliding mode control by the hyperbolic tangent function, and the chaos control performance was significantly improved. Besides, ABA Al-Hussein et al. [17] proposed an adaptive cooperative control strategy to realize the chaos suppression of power system with multiple control inputs based on multi-equipment. Furthermore, Wang et al. [18] combined finite time theory and function projection to design a chaos controller to synchronize the power system chaos model with the ideal model in a limited time, which indirectly realized the power system chaos control. Reference [19] proposed a sliding mode control method with the reaching law of the relay function, which can quickly suppress the chaos oscillation of the power system while significantly reducing the chatter. In summary, sliding mode control has relatively better chaos suppression performance, but in practical engineering, sliding mode control inevitably has chattering phenomenon, which seriously affects the operational stability of the system [20], [21]. Further, to deal with the nonlinear and uncertainties in the controlled systems, many advanced control strategies make use of neural network techniques. Sun et al. [22] proposed an amplitude saturation controller, which is improved based on the radial basis function neural networks to enhance effectiveness and robustness with respect to time delays. Liang et al. [23] designed a finite-time fault-tolerant control strategy with high accuracy, strong robustness, and anti-saturation based on the RBF neural network. In addition, Sun et al. [24] fused a radial basis function neural network into the basic controller, which has a robust control performance that is able to mitigate the uncertainty.

Based on the above discussion, this paper proposes a multivariate cooperative internal model control strategy based on RBF-NN inverse system, and applies it to ES and SVC to realize the control strategy of chaos suppression in power system considering their ability to regulate active and reactive power. Given that power system chaotic oscillation are highly sensitive to system parameters change and external disturbances, and chaotic oscillation will affect multiple state variables in the system, multivariate cooperative internal model control (IMC) is chosen because it has the advantages of no chattering, fast response, robustness, and convenient tuning, which is suitable for application in complex systems with strong coupling and multiple variables to suppress chaotic oscillation. Second, this paper decouples the pseudo-linearization of the multi-input and multi-output (MIMO) power system model into n single-input and single-output (SISO) subsystems according to the inverse system theory and neural network theory to realize the targeted control of the controlled variables and effectively suppress the chaotic oscillations of the power system with complex causes. In addition, since the power system has many uncertainties, and considering that RBF-NN has a very strong nonlinear fitting and fault tolerance ability, the inverse system model of the power system is fitted by RBF-NN instead of the mathematical expression, which reduces the sensitivity of the IMC to the change of the system parameters, and improves the stability of the controlled system and the robustness of the controller.

II. POWER SYSTEM MODEL AND CHAOS DYNAMICS ANALYSIS

A. ESTABLISHMENT OF SEVEN-DIMENSIONAL CONTROLLED MODEL OF POWER SYSTEM

The dynamic models of ES and SVC [14] are introduced to the classical four-dimensional model of a three-node power system [25] to establish the seven-dimensional controlled model of the power system, which consists of a generator G_1 representing the slack node, another generator G_2 with constant voltage amplitude, and a dynamic load. SVC and ES are used to control the system power, considering that in a real system, SVC can improve the power factor in the power system on the consumer side and ES can balance the power flow between the generator side and the consumer side, so ES_1 is installed on the generator G_2 busbar, and ES_2 and SVC are installed on the dynamic load busbar. The equivalent circuit of the power system is shown in Fig. 1.

The seven-dimensional controlled model of power system is shown in (1).

$$
\begin{cases}
\dot{\delta}_m = f_1(x) = \omega \\
\boldsymbol{M}\dot{\omega} = f_2(x) = -d_m\omega + P_m + E_m Y_m V \sin(\delta - \delta_m - \theta_m) \\
\qquad +E_m^2 Y_m \sin\theta_m - P_{ES1} \\
\dot{P}_{ES1} = -\dfrac{1}{T_{ES1}}P_{ES1} + \dfrac{K_{ES1}}{T_{ES1}}u_{ES1} = f_3(x) + \dfrac{K_{ES1}}{T_{ES1}}u_{ES1} \\
K_{q\omega}\dot{\delta} = f_4(x) = -K_{qv2}V^2 - K_{qv}V + E_0' Y_0' V\cos\left(\delta + \theta_0'\right) \\
\qquad +E_m Y_m V\cos\left(\delta - \delta_m + \theta_m\right) \\
\qquad -\left(Y_0'\cos\theta_0' + Y_m\cos\theta_m\right)V^2 - Q_0 - Q_1 - BV^2 \\
\dot{B} = -\dfrac{1}{T_{SVC}}B + \dfrac{K_{SVC}}{T_{SVC}}u_{SVC} = f_5(x) + \dfrac{K_{SVC}}{T_{SVC}}u_{SVC} \\
TK_{q\omega}K_{pv}\dot{V} = f_6(x) = K_{p\omega}K_{qv2}V^2 \\
\qquad +\left(K_{p\omega}K_{qv} - K_{q\omega}K_{pv}\right)V + K_{q\omega}\Big(-E_0' Y_0' V\sin\left(\delta + \theta_0'\right) \\
\qquad -E_m Y_m V\sin\left(\delta - \delta_m + \theta_m\right) \\
\qquad +\left(Y_0'\sin\theta_0' + Y_m\sin\theta_m\right)V^2 - P_0 - P_1 - P_{ES2}) \\
\qquad -K_{p\omega}\Big(E_0' Y_0' V\cos\left(\delta + \theta_0'\right) + E_m Y_m V\cos\left(\delta - \delta_m + \theta_m\right) \\
\qquad -\left(Y_0'\cos\theta_0' + Y_m\cos\theta_m\right)V^2 - Q_0 - Q_1 - BV^2\Big) \\
\dot{P}_{ES2} = -\dfrac{1}{T_{ES2}}P_{ES2} + \dfrac{K_{ES2}}{T_{ES2}}u_{ES2} = f_7(x) + \dfrac{K_{ES2}}{T_{ES2}}u_{ES2}
\end{cases}
\tag{1}
$$

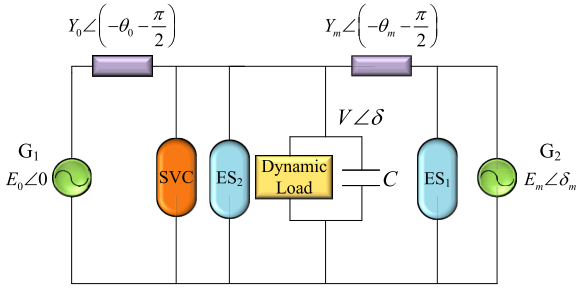

FIGURE 1. Equivalent circuit diagram of controlled power system.

where the state variables $x = [x_1, x_2, x_3, x_4, x_5, x_6, x_7]^T = [\delta_m, \omega, P_{ES1}, \delta, B, V, P_{ES2}]^T$ represent the power angle and the angle-frequency difference of the generator G_2, the active power absorbed by ES_1, the voltage angle of the load node, the susceptance of the SVC, the voltage amplitude of the load node and the active power absorbed by ES_2, respectively. Control inputs $u = [u_1, u_2, u_3]^T = [u_{ES1}, u_{SVC}, u_{ES2}]^T$. In addition, M is the angular momentum of the generator; d_m is the modified damping coefficient; P_m is the input mechanical power; E_m is the constant voltage amplitude of generator G_2; Y_m and θ_m are the magnitude and phase of the admittance between the generator G_2 and load busbar; $K_{p\omega}$, $K_{q\omega}$, K_{pv}, and K_{qv} are load coefficients, whose subscripts $p\omega$, $q\omega$, pv, and qv represent frequency dependence of the active load, frequency dependence of the reactive load, voltage dependence of the active load, and voltage dependence of the reactive load respectively; P_0 and Q_0 are the constant active and reactive powers of the induction motor in load; T is the time constant of the induction motor; P_1 and Q_1 are the active and reactive components of the dynamic load; E_0' is the Thevenin equivalent voltage amplitude of generator G_1; Y_0' and θ_0' are the Thevenin equivalent magnitude and phase of the admittance between the generator G1 and load busbar; T_{ES1}, T_{ES2}, and T_{SVC} are the time constants of ES_1, ES_2, and SVC; K_{ES1}, K_{ES2}, and K_{SVC} are the gains of ES_1, ES_2 and SVC. Then, the values of the parameters in the model are shown in Table 1 [14], [25]. Note that the parameters are per-unit values, except for the angles, which are in radians.

TABLE 1. Parameters of power system.

M	0.3	d_m	0.05	P_m	1.0	E_m	1.0
Y_m	5.0	θ_m	-5.0	$K_{q\omega}$	-0.03	K_{qv}	-2.8
Q_0	1.3	T	8.5	$K_{p\omega}$	0.4	K_{pv}	0.3
P_0	0.6	P_1	0.0	Q_1	11.3804	E_0'	2.5
Y_0'	8	θ_0'	-12.0	T_{ES1}	1.0	T_{ES2}	1.0
K_{ES2}	1.0	K_{ES1}	1.0	T_{SVC}	0.01	K_{SVC}	1.0

B. NONLINEAR DYNAMICS ANALYSIS OF POWER SYSTEM

Due to load variations or system parameter changes, the power system may be affected by load power disturbances, resulting in unstable bifurcation and chaos in the power system. Therefore, in this paper, a common low-frequency power disturbance is taken as a load power disturbance, focusing on analyzing the effects of the frequency and amplitude of the disturbance on the nonlinear dynamics of the power system. Then, the power system model with load power disturbance can be seen from (2).

$$\begin{cases} \dot{\delta}_m = f_1(x) \\ M\dot{\omega} = f_2(x) + P_k\cos(2\pi ft) \\ \dot{P}_{ES1} = f_3(x) + \dfrac{K_{ES1}}{T_{ES1}}u_{ES1} \\ K_{q\omega}\dot{\delta} = f_4(x) \\ \dot{B} = f_5(x) + \dfrac{K_{SVC}}{T_{SVC}}u_{SVC} \\ TK_{q\omega}K_{pv}\dot{V} = f_6(x) \\ \dot{P}_{ES2} = f_7(x) + \dfrac{K_{ES2}}{T_{ES2}}u_{ES2} \end{cases} \tag{2}$$

where P_k and f are the amplitude and frequency of the load power disturbance, respectively.

The initial value of the state variable of (2) is selected as $x_0 = [0.3492,0,0,0.1387,0,0.9181,0]^T$, and the control inputs are $u = [0,0,0]^T$. First, when the amplitude of the load power disturbance is small, the effect of the frequency of the power disturbance on the nonlinear dynamics of the power system is observed by fixing $P_k = 0.01$ and varying f within [1Hz, 4Hz], the local bifurcation diagram of the power system is shown in Fig. 2(a).

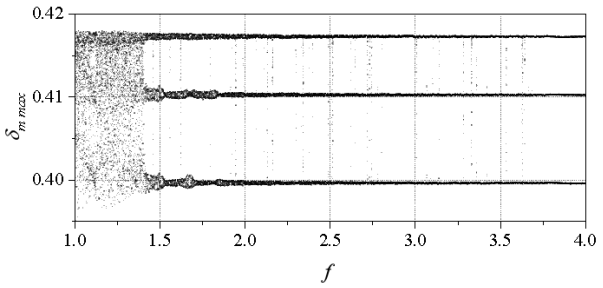

(a) Local bifurcation diagram with varying f

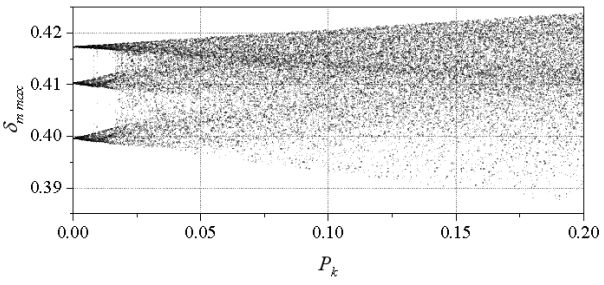

(b) Local bifurcation diagram with varying P_k

FIGURE 2. Local bifurcation diagram with varying low-frequency power disturbance.

From Fig. 2(a), it can be seen that when the frequency of the load power disturbance in the power system varies between [1.0 Hz, 1.402 Hz], chaotic phenomena appear in the system, and chaotic motion occurs in the power angle δ_m, voltage V and other state variables in the system. When f>1.402 Hz, a merging crisis occurs in the system, and the chaotic attractor splits from one to three, and as f continues to increase to 4Hz,

the system gradually behaves as a three-cycle limit loop, and this state also puts the electrical parameters in the system into a state of continuous oscillation.

In addition, fix $f = 1.5$ Hz and vary P_k within [0, 0.2] to observe the nonlinear dynamics change of the system as shown in Fig. 2 (b). When P_k is gradually increased at [0, 0.0171], the system changes from a three-cycle motion to a state of coexistence of three chaotic attractors, and when $P_k = 0.0172$, a merging crisis occurs to make the three chaotic attractors merge into one larger chaotic attractor, and the size of this chaotic attractor keeps increasing as P_k keeps increasing, indicating that the larger the amplitude of the low-frequency power disturbance, the greater the nonlinear dynamics of the power system.

Further, $P_k = 0.15$ and $f = 1.5$ Hz are chosen to plot the chaotic attractor phase diagrams and timing diagrams of the power system, as shown in Fig. 3 and Fig. 4. From Fig. 3, it can be seen that when the power system is in a chaotic state, the state variables of the system form a chaotic orbit around the equilibrium point with dimensionality, randomness and boundedness. In addition, Fig. 4 shows that the state variables of the system exhibit continuous irregular oscillations in the chaotic state, and this type of oscillation can seriously affect the operation of the power system, such as causing mechanical damage to generators, component damage to transmission lines, and even voltage collapse in the power system, which poses an obvious threat to the safety and stability of the power system.

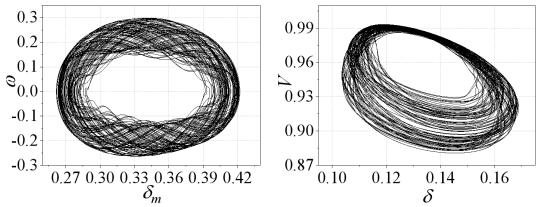

FIGURE 3. Attractor phase diagram between state variables (P_k=0.15, f=1.5Hz).

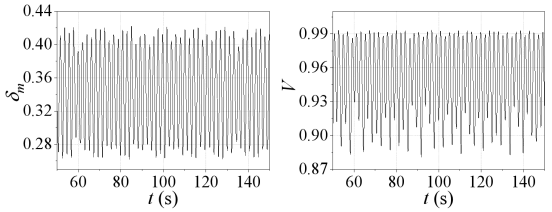

FIGURE 4. Timing diagram of δ_m and V (P_k=0.15, f=1.5Hz).

III. DESIGN OF MULTIVARIATE COOPERATIVE IMC BASED ON RBF-NN INVERSE SYSTEM

A. DESIGN OF RBF-NN INVERSE SYSTEM

In order to improve the control accuracy and to reduce the interactions between the subsystems of MIMO power system, (1) is subjected to nonlinear decoupling control, the key of which lies in the establishment of the corresponding inverse system. According to the Interator algorithm [26], the design steps of the inverse system of (1) are as follows:

1) SELECTION OF VARIABLES

Considering the power angle of generator and load voltage are significant indicators to measure the stability of the power system, decouple (1) into three SISO subsystems over them for high-performance control. Then, suppose the controlled state variables (controlled outputs) are δ_m, δ, and V:

$$y = [y_1, y_2, y_3]^T = [x_1, x_4, x_6]^T = [\delta_m, \delta, V]^T \tag{3}$$

Next, to enable effective control of both the generator and consumer sides, ES_1 on the generator G_2 busbar and SVC and ES_2 on the dynamic load busbar control δ_m, δ, and V respectively, so that u_{ES1}, u_{ES1}, and u_{ES2} are selected as control inputs:

$$u = [u_1, u_2, u_3]^T = [u_{ES1}, u_{SVC}, u_{ES2}]^T \tag{4}$$

2) ANALYSIS OF SYSTEM REVERSIBILITY

Reversibility is a necessary condition for the existence of an inverse system in a controlled system. First, the derivative is continuously derived for the controlled variable y_1 until the control input u is explicitly included in $y_1^{(\alpha_1)}$, as shown in (5).

$$\begin{cases} y_1^{(1)} = x_2 \\ y_1^{(2)} = \dfrac{f_2(x)}{M} \\ y_1^{(3)} = \dfrac{A_{11}\dot{x}_1 + A_{12}\dot{x}_2 + A_{13}\dot{x}_3 + A_{14}\dot{x}_4}{M} + \dfrac{A_{15}\dot{x}_5 + A_{16}\dot{x}_6 + A_{17}\dot{x}_7}{M} \\ \quad = \dfrac{F_1 + A_{13}(f_3(x) + K_{ES1}u_1/T_{ES1})}{M} \end{cases} \tag{5}$$

where:

$A_{11} = -E_m Y_m \cos(x_4 - x_1 - \theta_m)x_6$,
$A_{12} = -d_m$, $A_{13} = -1$, $A_{17} = 0$,
$A_{14} = E_m Y_m \cos(x_4 - x_1 - \theta_m)x_6$,
$A_{15} = 0$, $A_{16} = E_m Y_m \sin(x_4 - x_1 - \theta_m)$

Also, the derivative is continuously derived for the controlled variable y_2 until the control input u is explicitly included in $y_2^{(\alpha_2)}$, as shown in (6).

$$\begin{cases} y_2^{(1)} = \dfrac{f_4(x)}{K_{q\omega}} \\ y_2^{(2)} = \dfrac{A_{21}\dot{x}_1 + A_{22}\dot{x}_2 + A_{23}\dot{x}_3 + A_{24}\dot{x}_4}{K_{q\omega}} + \dfrac{A_{25}\dot{x}_5 + A_{26}\dot{x}_6 + A_{27}\dot{x}_7}{K_{q\omega}} \\ \quad = \dfrac{F_2 + A_{25}(f_5(x) + K_{SVC}u_2/T_{SVC})}{K_{q\omega}} \end{cases} \tag{6}$$

where:

$A_{21} = E_m Y_m \sin(x_4 - x_1 + \theta_m)x_6$,
$A_{22} = 0$, $A_{23} = 0$, $A_{27} = 0$,
$A_{24} = -[E_0' Y_0' \sin(x_4 + \theta_0') + E_m Y_m \sin(x_4 - x_1 + \theta_m)]x_6$,
$A_{25} = -x_6^2$,

$$A_{26} = -2K_{qv2}x_6 - K_{qv} + E'_0Y'_0\cos(x_4 + \theta'_0) + E_mY_m\cos(x_4 - x_1 + \theta_m) - 2(Y'_0\cos\theta'_0 + Y_m\cos\theta_m)x_6 - 2x_5x_6$$

Then, the derivative is continuously derived for the controlled variable y_3 until the control input u is explicitly included in $y_3^{(\alpha_3)}$, as shown in (7).

$$\begin{cases} y_3^{(1)} = \dfrac{f_6(x)}{TK_{q\omega}K_{pv}} \\ y_3^{(2)} = \dfrac{A_{31}\dot{x}_1 + A_{32}\dot{x}_2 + A_{33}\dot{x}_3 + A_{34}\dot{x}_4}{TK_{q\omega}K_{pv}} \\ \qquad \dfrac{A_{35}\dot{x}_5 + A_{36}\dot{x}_6 + A_{37}\dot{x}_7}{TK_{q\omega}K_{pv}} \\ \qquad = \dfrac{F_3 + A_{37}\left(f_7(x) + K_{ES2}u_3/T_{ES2}\right)}{TK_{q\omega}K_{pv}} \end{cases} \tag{7}$$

where:

$$\begin{aligned} A_{31} &= [K_{q\omega}\cos(x_4 - x_1 + \theta_m) \\ &\quad - K_{p\omega}\sin(x_4 - x_1 + \theta_m)]E_mY_mx_6, \\ A_{32} &= 0, A_{35} = -K_{q\omega}, A_{37} = K_{p\omega}x_6^2, \\ A_{34} &= -K_{q\omega}[E'_0Y'_0\cos(x_4 + \theta'_0) \\ &\quad + E_mY_m\cos(x_4 - x_1 + \theta_m)]x_6 \\ &\quad + K_{p\omega}[E'_0Y'_0\sin(x_4 + \theta'_0) \\ &\quad + E_mY_m\sin(x_4 - x_1 + \theta_m)]x_6, \\ A_{36} &= 2K_{p\omega}K_{qv2}x_6 + (K_{p\omega}K_{qv} - K_{q\omega}K_{pv}) \\ &\quad - K_{q\omega}[E'_0Y'_0\sin(x_4 + \theta'_0) + E_mY_m\sin(x_4 - x_1 + \theta_m) \\ &\quad - 2(Y'_0\sin\theta'_0 + Y_m\sin\theta_m)x_6 - 2x_5x_6] \\ &\quad - K_{p\omega}[E'_0Y'_0\cos(x_4 + \theta'_0) + E_mY_m\cos(x_4 - x_1 + \theta_m) \\ &\quad - 2(Y'_0\cos\theta'_0 + Y_m\cos\theta_m)x_6 - 2x_5x_6] \end{aligned}$$

According to (5), (6), and (7), $\alpha = [\alpha_1, \alpha_2, \alpha_3]^T = [3, 2, 2]^T$, which are defined as the relative orders. In addition, the Jacobain matrix J and its determinant $|J|$ corresponding to $y_i^{(\alpha_i)}(i = 1, 2, 3)$ are:

$$J = \begin{bmatrix} \frac{\partial y_1^{(3)}}{\partial u_1} & \frac{\partial y_1^{(3)}}{\partial u_2} & \frac{\partial y_1^{(3)}}{\partial u_3} \\ \frac{\partial y_2^{(2)}}{\partial u_1} & \frac{\partial y_2^{(2)}}{\partial u_2} & \frac{\partial y_2^{(2)}}{\partial u_3} \\ \frac{\partial y_3^{(2)}}{\partial u_1} & \frac{\partial y_3^{(2)}}{\partial u_2} & \frac{\partial y_3^{(2)}}{\partial u_3} \end{bmatrix} = \begin{bmatrix} \frac{-K_{ES1}}{MT_{ES1}} & 0 & 0 \\ 0 & \frac{-K_{SVC}x_6^2}{K_{q\omega}T_{SVC}} & 0 \\ 0 & \frac{K_{p\omega}K_{SVC}x_6^2}{TK_{q\omega}K_{pv}T_{SVC}} & \frac{-K_{ES2}}{TK_{pv}T_{ES2}} \end{bmatrix} \tag{8}$$

$$|J| = -\frac{-K_{ES1}K_{SVC}K_{ES2}x_6^2}{MK_{q\omega}T_{SVC}TK_{pv}T_{ES1}T_{ES2}} \tag{9}$$

Since $x_6 \neq 0$ in the system workspace, the Jacobain matrix J is full rank, and its determinant $|J| \neq 0$, that is, J is non-singular. Moreover, the sum of relative orders of the contrilled system is $\alpha_1 + \alpha_2 + \alpha_3 = 7$, which is equal to the dimension of the controlled system (1). Thus, according to reference [26], the controlled system is reversible.

Further, transform (5), (6), and (7) to obtain the expression of the inverse system Φ as follows, in which the control outputs and their derivatives are used to represent the control inputs the of inverse system:

$$\begin{aligned} u &= (u_1, u_2, u_3)^T \\ &= \Phi\left(y_1^{(3)}, y_2^{(2)}, y_3^{(2)}, y_1, y_1^{(1)}, y_1^{(2)}, y_2, y_2^{(1)}, y_3, y_3^{(1)}\right) \end{aligned} \tag{10}$$

3) RBF-NN FITTING INVERSE SYSTEM

Since the construction of mathematical models of controlled objects in practical engineering is affected by uncertainties and leads to inaccuracies, the identification of inverse systems by input and output data can improve the construction of inverse systems. Since (10) is extremely nonlinear and its establishment depends on the certainty of the controlled system model, and the power system is affected by many uncertainties in actual operation, considering that RBF-NN has excellent nonlinear fitting ability and generalization performance, RBF-NN is used to fit (10) in order to improve the accuracy and stability of the inverse system.

RBF neural networks have an input layer, a hidden layer, and an output layer [27]. The output from the input layer d to the hidden layer is a nonlinear activation function $h_j(t)$:

$$h_j(t) = \exp\left[-\frac{\|X(t) - C_j(t)\|^2}{2\sigma_j^2}\right], \quad j = 1, 2, \cdots, m \tag{11}$$

where $X(t)$ is input vector, $C_j$is the center vector of the j- th implicit layer node, m is the number of implicit layer nodes, and σ_j is the width of the Gaussian basis function.

Moreover, the output Y from the implicit layer to the output layer is implemented by weighting as follows:

$$Y_i(t) = \sum_{j=1}^{m} \varepsilon_{ji}h_j(t), \quad i = 1, 2, \cdots, n \tag{12}$$

where ε is the weight of the output layer and n is the number of nodes in the output layer.

Fig. 5 plots a schematic of the RBF-NN fitted inverse system: sufficient uniform random signals are input to excite the input-output characteristics of the inverse system, and the RBF-NN model is trained using the obtained inputs and outputs to obtain the RBF-NN inverse system.

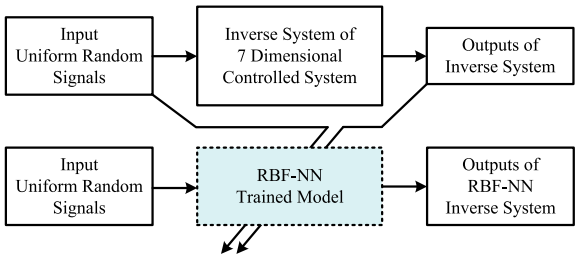

FIGURE 5. Schematic diagram of the RBF-NN fitted inverse system.

Further, after fitting the inverse system by RBF-NN, the RBF-NN inverse system is connected before the controlled system (1) to form a pseudo-linear composite system

that decouples the MIMO power system into three SISO pseudo-linear subsystems with respect to the controlled variables:

$$G_i(s) = s^{-\alpha_i}, \quad i = 1, 2, 3 \tag{13}$$

Then the schematic diagram of the pseudo-linear decoupling process is shown in Fig. 6, where $[\, y_1^{(3)}, y_2^{(2)}, y_3^{(2)}, y_1, y_1^{(1)}, y_1^{(2)}, y_2, y_2^{(1)}, y_3, y_3^{(1)}]^T = [\, v_1, v_2, v_3, z_{10}, z_{11}, z_{12}, z_{20}, z_{21}, z_{30}, z_{31}]^T$.

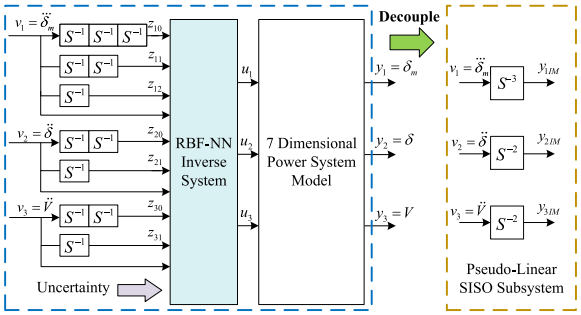

FIGURE 6. Schematic diagram of the pseudo-linear decoupling process.

Meanwhile, in order to verify the output consistency of the established RBF-NN pseudo-linear composite system with the pseudo-linear SISO subsystem, we analyzed the output error between the two, as shown in Fig. 7. It can be seen that the error between the output of the RBF-NN pseudo-linear composite system (y) and the output of the pseudo-linear SISO subsystem (y_{IM}) is almost zero when the input signals are the same, indicating the feasibility of the RBF-NN inverse system.

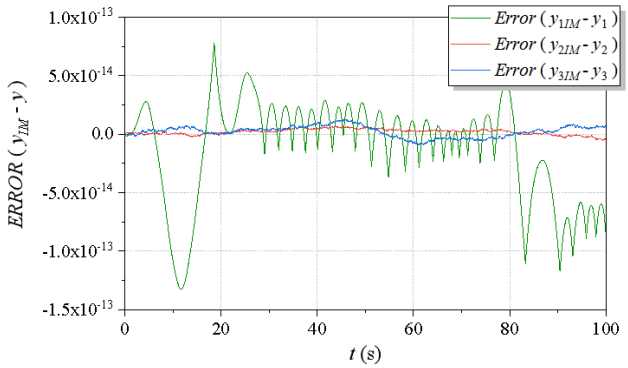

FIGURE 7. Error curves between y_{IM} and y when using RBF-NN inverse system.

B. DESIGN OF MULTIVARIATE COOPERATIVE IMC

The basic idea of multivariate cooperative IMC is to parallelize a controlled system with a matching internal model and use the difference of its outputs to feed back to the controller input, so that multiple controlled variables are stabilized at the target operating point. Therefore, combining the pseudo-linear composite system with the pseudo-linear SISO subsystem, the control structure is shown in Fig. 8.

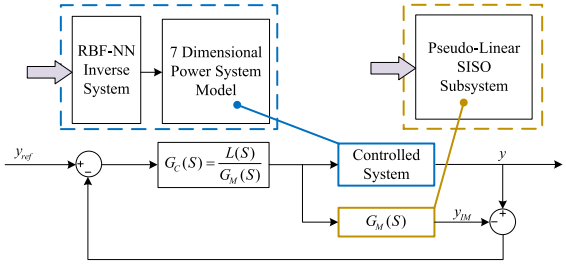

FIGURE 8. Control structure of multivariate cooperative IMC based on RBF-NN inverse system.

Where $G_C(S)$ is multivariate cooperative IMC controller, $G_M(S)$ is internal model, $L(S)$ is IMC controller, y_{ref} is tracking signal for control, and y is controlled output.

According to SISO pseudo-linear subsystems (13), the internal model can be expressed as:

$$G_{Mi}(S) = G_i(S), \quad i = 1, 2, 3 \tag{14}$$

Introduce inertia element to construct controller, and λ is the controller parameter:

$$L_i(S) = \frac{1}{(\lambda_i S + 1)^{\alpha_i}}, \quad i = 1, 2, 3 \tag{15}$$

where α_i is equal to the corresponding α value in (13).

Then, combining (14) and (15), the multivariate cooperative IMC controller is obtained as follows:

$$G_{Ci}(S) = \frac{S^{\alpha_i}}{(\lambda_i S + 1)^{\alpha_i}}, \quad i = 1, 2, 3 \tag{16}$$

Further, according to (14) and (15), the error equation of the control system can be obtained from Fig. 8:

$$E_i(S) = \frac{1 - L_i(S)}{1 + L_i(S)\, G_{Mi}^{-1}(S)\, [G_P(S) - G_{Mi}(s)]} R(S)$$
$$i = 1, 2, 3 \tag{17}$$

Substituting (15) into (17) gives:

$$E_i(S) = \frac{(\lambda_i S + 1)^{\alpha_i} - 1}{(\lambda_i S + 1)^{\alpha_i} + l_m(S)} R(S), \quad i = 1, 2, 3 \tag{18}$$

where $G_P(S)$ is the transfer function of controlled system in Fig. 8, that has been shown to have an upper error bound $l_m(S)$ [28].

Set $\lim_{S \to 0} l_m(S) = C$ (constant), then:

1) If $R(S) = r_0/S$, then the final error of the system after the controlled is $e(\infty) = \lim_{S \to 0} S \left[\frac{(\lambda_i S+1)^{\alpha_i} - 1}{(\lambda_i S+1)^{\alpha_i} + l_m(S)} \frac{r_0}{S} \right] = 0$;

2) If $R(S) = r_0/S^2$, then the final error of the system after the controlled is $e(\infty) = \lim_{S \to 0} S \left[\frac{(\lambda_i S+1)^{\alpha_i} - 1}{(\lambda_i S+1)^{\alpha_i} + l_m(S)} \frac{r_0}{S^2} \right] = \frac{\alpha_i \lambda_i r_0}{1+C}$, which is a constant.

Therefore, as long as the value of λ_i is small, the step and ramp signals can be tracked with high accuracy by introducing an IMC structure into the controlled system based on Fig. 8, using a filter as in (15). From the above analysis,

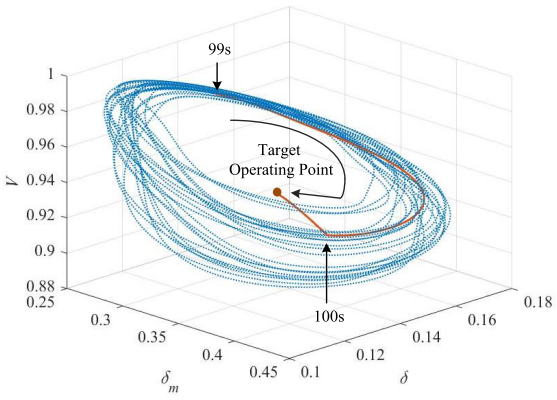

FIGURE 9. The attractor phase diagram before and after adding the designed controller.

the controller (16) is theoretically able to suppress the chaotic oscillations of the power system and keep the system stable.

IV. SIMULATION ANALYSIS

In this paper, a multivariate cooperative IMC based on the RBF-NN inverse system is used to simulate power system (2) with chaotic behavior due to the low-frequency power disturbance that P_k=0.15 and f=1.5 Hz are chosen, and the state of power system is shown in Fig. 3 and Fig. 4.

The initial value of the state variable of (2) is selected as $x_0 = [0.3492,0,0,0.1387,0,0.9181,0]^T$, the target operating point is $y_{ref} = [0.346,0.1371,0.9318]^T$, and controller parameters are $\lambda = [0.01,0.01,0.01]^T$. Then, the designed controller is added at the 100-th s of system (2) operation, and its attractor phase diagram is shown in Fig. 9.

It can be seen from Fig. 9 that the power system exhibits chaotic attractor with complex and chaotic orbit in the first 100s, which reveals that the power system is in an extremely unstable operating state around the equilibrium point. Then, when the designed controller is added in the 100-th s, the chaotic attractor disappears and the state of the system quickly and steadily reaches the set target operating point from the chaotic orbit, demonstrating the effectiveness of the designed controller.

In addition, Fig. 10 shows the timing diagrams of the controlled variables δ_m, δ, and V before and after adding the designed controller, which shows that the state variables of the system show continuous chaotic oscillations when the controller is not added, and the oscillating state variables stabilize to the fixed point immediately after adding the controller, and the control effect is smooth after 100s without any chattering. Meanwhile, Fig. 11 shows the power characteristics of ES_1, ES_2 and SVC after the power system is under control, which can show that P_{ES1}, P_{ES2}, and B can achieve stability, and Fig. 11 also shows that the ES absorbs part of the active power in the controlled system and the SVC compensates the reactive power to maintain the power balance in the system to eliminate the chaotic oscillations.

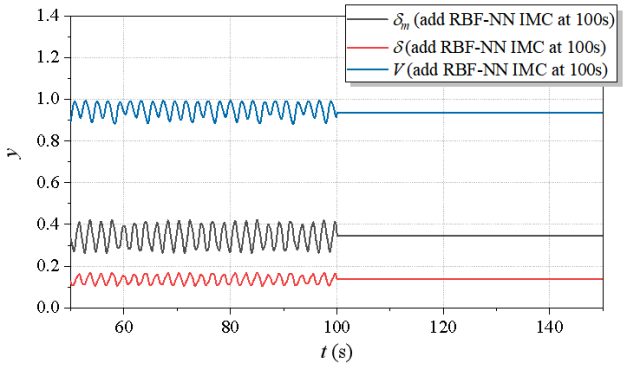

FIGURE 10. Timing diagrams of the controlled variables before and after adding the designed controller.

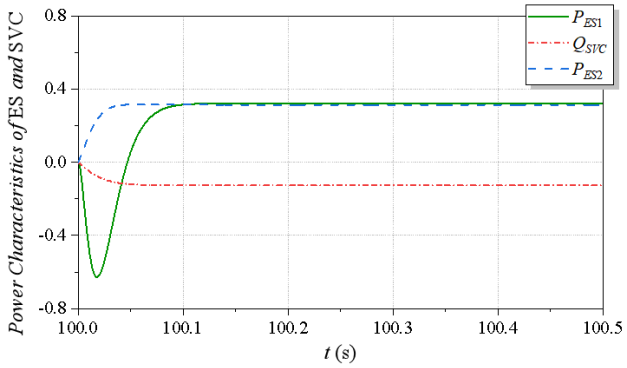

FIGURE 11. Power characteristics of ES and SVC after power system control.

Then, to further illustrate the superiority of the designed controller, we partially zoom in on Fig. 10 and compare it with the control strategy in the reference [19] and reference [29]. Then, the results are showed in Fig. 12 (a), Fig. 12 (b), and Fig. 12 (c). Note that control strategy 1 represents proposed control method in this paper, control strategy 2 represents the approach of the reference [29], and control strategy 3 represents the approach of the reference [19]. As can be seen from Fig. 12, all control strategies allow the power system to reach the target operating point (red dotted lines) from the chaotic state within 1s with almost no overshoot. However, the proposed control method allows the controlled variables to enter into stabilization approximately at A1 (100.075s), A2 (100.077s), and A3 (100.077s), whereas control strategy 2 at B1 (100.524s), B2 (100.519s), and B3 (100.519s), and control strategy 3 at C1 (100.263s), C2 (100.249s), and C3 (100.249s). It is obvious that control strategy 1 has the fastest convergence speed among the three strategies, which can guarantee the stable operation of the power system.

Furthermore, to test the low sensitivity of the proposed control strategy to parameter mutations, this paper increases the load reactive power Q_1 to 11.3904 at the 101-th s to intervene in the controlled power system, and the results are shown in Fig. 12. According to (2), since the change of the load reactive power has a small effect on the generator power angle δ_m, Fig. 12 (a) shows that both control strategies are

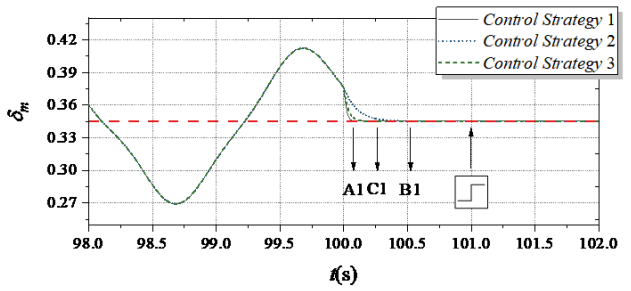

(a) Timing diagram of the controlled response of δ_m

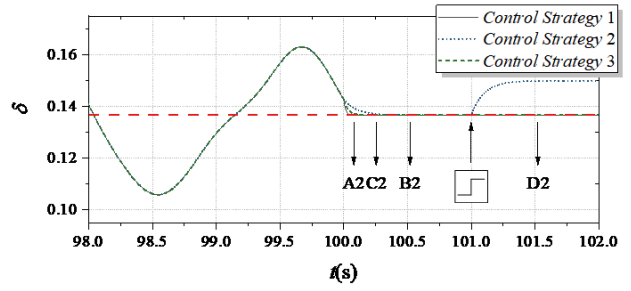

(b) Timing diagram of the controlled response of δ

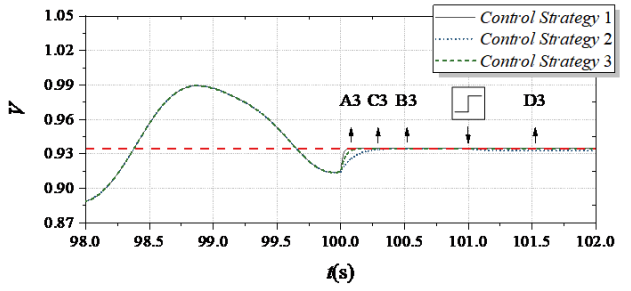

(c) Timing diagram of the controlled response of V

FIGURE 12. Timing comparison diagrams of controlled variables with two control strategies.

able to keep δ_m stable when the intervention occurs. However, since the load reactive power can directly affect the dynamics of the angle δ and magnitude V of the voltage at the load node, and the increase of Q_1 brings the power system closer to the limit point, which reduces the voltage stability, in Fig. 12 (b) and (c), control strategy 2 is not able to keep δ and V tracking the reference values at the time of the intervention occurrence plainly, and instead they are re-stabilized at another fixed point at D2 (101.529s) and D3 (101.525s) approximately with error 9.8% and 5.2% respectively. In addition, at the 101-th s, control strategy 3 also produces a tiny tracking error of almost 0.2% evenly, which can be ignored. However, in practice, due to the extremely high nonlinearity of the power system, even small parameter errors can trigger or even exacerbate its nonlinear behaviour, which must be avoided. As a comparison, the generalisation capability of RBF-NN enables the designed inverse system of the power system to quickly deal with the uncertainties arising from sudden changes in the load reactive power, and therefore the proposed control strategy (control strategy 1) is able to keep δ and V stabilized at the reference values in the face of sudden changes in the system parameters, suggesting that it has low parameter sensitivity and high robustness to ensure the stability of the power system.

V. CONCLUSION

In this paper, based on the nonlinear theory, the chaotic phenomenon generated by the seven-dimensional model of power system containing SVC and ES when low-frequency power disturbance is applied is analyzed, and secondly, a multivariate cooperative IMC strategy based on RBF-NN is designed for this problem by combining SVC and ES, and the following conclusions are obtained:

1)If the frequency of the applied low-frequency power disturbance is less than 1.402 Hz or the amplitude is greater than 0.0172, there is a high probability of chaotic behavior in the power system, which is manifested by irregular oscillations of the system state variables.

2)The fitting of RBF-NN to the inverse system of the power system has high accuracy and can provide an effective solution to the real power system in pseudo-linearization decoupling.

3)The multivariate cooperative IMC strategy based on the RBF-NN inverse system has a significant suppression effect on chaotic oscillations in power system, and can quickly stabilize the system state at the target operating point with smooth and no-chattering control effects.

Chaotic behavior is a potential threat to the stable operation of the power system, while the proposed control strategy with SVC and ES can make an effective response to it, thus improving the stability and safety of the power system.

REFERENCES

[1] Z. Liu, *Chaotic Dynamics and Its Application*. Beijing, China: Higher Education Press, 2006, pp. 4–8.

[2] M. Hallaji, A. Dideban, and M. A. Khanesar, "Optimal synchronization of non-smooth fractional order chaotic systems with uncertainty based on extension of a numerical approach in fractional optimal control problems," *Chaos, Solitons Fractals*, vol. 115, pp. 325–340, Oct. 2018, doi: 10.1016/j.chaos.2018.07.024.

[3] X. D. Wang and Y. S. Chen, "Bifurcation and singularity analysis of a class of power systems," *J. Vibrat. Shock*, vol. 33, no. 4, pp. 1–9, Feb. 2014, doi: 10.13465/j.cnki.jvs.2014.04.001.

[4] Z. X. Gong, A. Yaermaimaiti, H. Xin, W. Wang, X. Zhang, D. Chen, G. Z. Yang, C. R. Yang, and H. T. Hu, "Small-disturbance stability analysis of grid-connected equipment in new energy power system (1): Mechanism model and applicability of stability criterion?" *J. Chin. Electr. Eng. Sci.*, vol. 42, no. 12, pp. 1–16, 2022.

[5] N. Xize and Q. Jiajun, "Investigation of torsional instability, bifurcation, and chaos of a generator set," *IEEE Trans. Energy Convers.*, vol. 17, no. 2, pp. 164–168, Jun. 2002, doi: 10.1109/TEC.2002.1009463.

[6] X. Chen, W. Zhang, and W. Zhang, "Chaotic and subharmonic oscillations of a nonlinear power system," *IEEE Trans. Circuits Syst. II, Exp. Briefs*, vol. 52, no. 12, pp. 811–815, Dec. 2005, doi: 10.1109/TCSII.2005.853512.

[7] J. B. Wang, L. Liu, and C. X. Liu, "Dynamic surface sliding mode control of chaotic oscillation in seventh order power systems," *J. Electr. Machinery Control*, vol. 25, no. 4, pp. 1–8, 2021, doi: 10.15938/j.emc.2021.04.001.

[8] L. Zhou and F. Chen, "Chaotic dynamics for a class of single-machine-infinite bus power system," *J. Vibrat. Control*, vol. 24, no. 3, pp. 582–587, Feb. 2018, doi: 10.1177/1077546316645225.

[9] J. Ma, Y. Sun, X. Yuan, J. Kurths, and M. Zhan, "Dynamics and collapse in a power system model with voltage variation: The damping effect," *PLoS ONE*, vol. 11, no. 11, Nov. 2016, Art. no. e0165943, doi: 10.1371/journal.pone.0165943.

[10] H. Ma, F. Min, G. Huang, and Y. Dou, "Chaos and bifurcation behavior in a fundamental power system with electromagnetic disturbance and load disturbance," *AIP Adv.*, vol. 9, no. 4, Apr. 2019, Art. no. 045017, doi: 10.1063/1.5087977.
[11] X. T. Li, J. B. Wang, L. Liu, Y. Wang, and C. X. Liu, "Controlling chaos in a six-dimensional power system model," in *Proc. Chin. Autom. Congr. (CAC)*, Nov. 2019, pp. 764–769, doi: 10.1109/cac48633.2019.8997047.
[12] C. Ai, S. He, and X. Fan, "Parameter estimation of fractional-order chaotic power system based on lens imaging learning strategy state transition algorithm," *IEEE Access*, vol. 11, pp. 13724–13737, 2023, doi: 10.1109/ACCESS.2023.3243081.
[13] J. Wang, L. Liu, C. Liu, and J. Liu, "Fixed-time synergetic control for a seven-dimensional chaotic power system model," *Int. J. Bifurcation Chaos*, vol. 29, no. 10, Sep. 2019, Art. no. 1950130, doi: 10.1142/S021812741950130X.
[14] J. Ni, L. Liu, C. Liu, X. Hu, and S. Li, "Fast fixed-time nonsingular terminal sliding mode control and its application to chaos suppression in power system," *IEEE Trans. Circuits Syst. II, Exp. Briefs*, vol. 64, no. 2, pp. 151–155, Feb. 2017, doi: 10.1109/TCSII.2016.2551539.
[15] Q. Cao and D. Q. Wei, "Dynamic surface sliding mode control of chaos in the fourth-order power system," *Chaos, Solitons Fractals*, vol. 170, May 2023, Art. no. 113420, doi: 10.1016/j.chaos.2023.113420.
[16] D. Zhu, W. Zhang, C. Liu, and J. Duan, "Fractional-order hyperbolic tangent sliding mode control for chaotic oscillation in power system," *Math. Problems Eng.*, vol. 2021, pp. 1–10, May 2021, doi: 10.1155/2021/6691941.
[17] A.-B.-A. Al-Hussein, F. R. Tahir, A. Ouannas, T.-C. Sun, H. Jahanshahi, and A. A. Aly, "Chaos suppressing in a three-buses power system using an adaptive synergetic control method," *Electronics*, vol. 10, no. 13, p. 1532, Jun. 2021, doi: 10.3390/electronics10131532.
[18] C. Wang, H. L. Zhang, and P. Ma, "Finite-time function projective synchronization control method for a chaotic power system," *J. Vibrat. Shock*, vol. 40, no. 14, pp. 125–131, 2021, doi: 10.13465/j.cnki.jvs.2021.14.017.
[19] Y. Lv, Y. Zhang, Q. Liu, S. Wang, and D. Shi, "Sliding mode control of two-parameter fourth-order chaos model of power system," *IEEE Trans. Circuits Syst. II, Exp. Briefs*, vol. 69, no. 12, pp. 4849–4853, Dec. 2022, doi: 10.1109/TCSII.2021.3062466.
[20] Y. Xu, S. Li, and J. Zou, "Integral sliding mode control based deadbeat predictive current control for PMSM drives with disturbance rejection," *IEEE Trans. Power Electron.*, vol. 37, no. 3, pp. 2845–2856, Mar. 2022, doi: 10.1109/TPEL.2021.3115875.
[21] Z. Li, F. Wang, D. Ke, J. Li, and W. Zhang, "Robust continuous model predictive speed and current control for PMSM with adaptive integral sliding-mode approach," *IEEE Trans. Power Electron.*, vol. 36, no. 12, pp. 14398–14408, Dec. 2021, doi: 10.1109/TPEL.2021.3086636.
[22] Y. Sun, J. Xu, G. Lin, W. Ji, and L. Wang, "RBF neural network-based supervisor control for Maglev vehicles on an elastic track with network time delay," *IEEE Trans. Ind. Informat.*, vol. 18, no. 1, pp. 509–519, Jan. 2022, doi: 10.1109/TII.2020.3032235.
[23] S. Liang and Y. Zhang, "Intelligent attitude fault-tolerant control of space tumbling target fly-around based on RBF neural network," *IEEE Access*, vol. 11, pp. 6610–6622, 2023, doi: 10.1109/ACCESS.2023.3237565.
[24] Y. Sun, J. Q. Xu, G. B. Lin, and N. Sun, "Adaptive neural network control for Maglev vehicle systems with time-varying mass and external disturbance," *Neural Comput. Appl.*, vol. 35, no. 17, pp. 12361–12372, 2023, doi: 10.1007/s00521-021-05874-2.
[25] I. Dobson and H.-D. Chiang, "Towards a theory of voltage collapse in electric power systems," *Syst. Control Lett.*, vol. 13, no. 3, pp. 253–262, Sep. 1989, doi: 10.1016/0167-6911(89)90072-8.
[26] X. Dai, *Interactor Algorithm in Neural Network Inverse Control Method for Multivariate Nonlinear Systems*. Beijing, China: Science Press, 2006, pp. 30–37.
[27] L. Li, X. H. Yang, L. Cao, and Y. J. Han, "Energy consumption prediction of building electricity based on improved RBF neural network," *Building Energy Efficiency*, vol. 49, no. 1, pp. 81–139, 2021.
[28] Q. Chen, Z. X. Lyu, W. L. Hu, and H. X. Wu, "Nonlinear internal model control based on inverse system method," *ACTA Autom. Sinica*, vol. 28, no. 5, pp. 715–721, 2002, doi: 10.16383/j.aas.2002.05.006.
[29] Y. Ma, S. Chen, and B. L. Zhang, "A study on nonlinear SVC control for improving power system stability," *J. Tsinghua Univ., Natural Sci. Ed.*, vol. 34, no. 4, pp. 1–8, 1993, doi: 10.1109/tencon.1993.320610.

ZHIPENG LIU was born in Heilongjiang, China, in 1989. He received the M.S. degree from the Harbin University of Science and Technology, Harbin, China. He is currently an engineer. His main research interests include machine and network coordination technology, new power generation technology, secondary system control, and fault monitoring.

YUCHEN ZHANG was born in Liaoning, China, in 1994. He received the M.S. degree from the Department of Electrical and Electronic Engineering, Harbin University of Science and Technology, Harbin, China, in 2021, where he is currently pursuing the Ph.D. degree in power system and automation with the Department of Electrical and Electronic Engineering. His current research interests include power system operation, control, and nonlinear analysis.

SHIJIE YANG was born in Hubei, China, in 1991. She received the M.S. degree from the Department of Electrical and Electronic Engineering, Harbin University of Science and Technology, Harbin, China, in 2018. Her main current research interests include power system fault and analysis and motor operation protection.

YANLING LYU was born in Heilongjiang, China, in 1975. She received the Ph.D. degree in electrical engineering from the Harbin University of Science and Technology (HUST), Harbin, China, in 2010. Currently, she is a Professor with HUST. Her research focuses on the operation and protection of large generators, generators and its system operation analysis, and power system fault and protection analyses.